ETH zürich

Institut für Baustatik und
Konstruktion - Holzbau

Vorgespannte Brettschichtholzträger

Erweiterung der Möglichkeiten im modernen Holzbau.
Fachlicher Schlussbericht

Dr. Marcel Muster, Prof. Dr. Andrea Frangi
03. Dezember 2023

Finanziert durch Wald- und Holzforschungsforderung Schweiz
WHFF-CH

Inhaltsverzeichnis

Zusammenfassung

Um wirtschaftliche Lösungen für weitgespannte Träger aus Holz anbieten zu können, wurde im Forschungsprojekt «Vorgespannte Brettschichtholzträger - Erweiterung der Möglichkeiten im modernen Holzbau» eine aus dem Stahlbetonbau bekannte Technologie auf Holzträger angewendet. Die Vorspannung wurde entweder mit oder ohne Verbund aufgebracht. Die total 11 getesteten Träger mit Spannweiten von 7.2, resp. 10.5 m zeigten ein gutmütiges Versagen und erreichten eine höhere Biegesteifigkeit von 12% (ohne Verbund) und 21% (mit Verbund) und eine höhere Tragfähigkeit von 58% (ohne Verbund) und 78% (mit Verbund) im Vergleich zu nicht vorgespannten Trägern.

Afin de proposer des solutions économiques pour les poutres en bois de grande portée, le projet de recherche «Poutres précontraintes en bois lamellé-collé - Elargissement des possibilités dans la construction moderne en bois» utilise, pour des poutres en bois, une technologie largement répandue dans la construction en béton. La précontrainte a été appliquée avec ou sans adhérence. Les 11 poutres testées, d'une portée de 7,2 et 10,5 m respectivement, ont montré une bonne résistance à la rupture et ont atteint une résistance à la flexion supérieure de 12% (sans adhérence) et 21% (avec adhérence) et une capacité portante supérieure de 58% (sans adhérence) et 78% (avec adhérence) par rapport aux poutres non précontraintes.

1 Introduction

1.1 Motivation and background

Structural timber engineering has undergone a rapid development in the past decades. As a result of the advances regarding engineered timber products, fastener technology, and application standards, timber has established itself as a technically, economically, and ecologically competitive construction material in numerous fields of applications. In wide-span ceiling and roof structures, timber trusses represent a material- and cost-efficient construction method. In situations where the girder height needs to be minimized, glulam or laminated veneer lumber (LVL) beams with solid cross sections are used. For such beams, the serviceability limit state (SLS), i.e., the deflections and/or floor vibrations, are usually governing the design, whereas the ultimate limit state (ULS) is usually only exploited by about 40 to 60%. Thus, the material itself cannot be utilized in an efficient manner.

In order to achieve a favorable stress state in the structural member and to compensate a controllable part of the deformations, post-tensioning of beams with parabolic, internal tendons has proven its efficiency in concrete construction.

In timber construction, however, this technology has hardly been applied in practise. Experimental investigations on the subject have been very limited so far and many of the research results are not publicly available.

The present report summarizes the investigations on the bonding behavior of different grouting systems, i.e., the composite effect of timber, mortar or adhesive, duct, and tendons observed in push- and pull-out tests. Secondly, the bending behavior of post-tensioned glulam beams with and without bonding as observed in four-point bending tests is presented. Finally, recommendations for the calculation and design of parabolically post-tensioned glulam beams are given. A major focus is on trans-parently presenting the challenges and lessons learned in the production and testing of post-tensioned glulam beams with parabolic tendons.

1.2 State-of-the-art

Despite the seemingly obvious advantages, post-tensioning (PT) of timber beams with internal parabolic tendons is far from being an established construction method. Rug and Pötke (1988) give a summary of early research projects conducted on the subject between 1950 and 1980. Themselves investigated the load-bearing and fracture behavior of PT glulam beams with and without bonding. The PT beams without bonding showed an increase in bending resistance compared to non-post-tensioned beams. However, shear failures around the PT were the governing failure mechanism. For beams featuring a bonding with polyester resin, a further increase in the load-bearing capacity was observed.

Among others, Newcombe et al. (2010), Buchanan et al. (2011), Wanninger (2015), and Ogrizovic (2019) investigated post-tensioned frame constructions made of LVL and glulam, respectively. Mainly focusing on the lateral behavior and resistance to horizontal loads induced by earthquakes, the system developed in New Zealand has been further developed and applied since then and the system studied in Switzerland was successfully used in the House of Natural Resources (HoNR) project in the form of internally post-tensioned frame joints at ETH Zurich.

Two research projects investigated the load-bearing and deformation behavior of board layers and glulam beams reinforced with post-tensioned round steel. Four-point bending tests were carried out on beams with a length of 3 m by McConnell et al. (2014) and with a length of 2 m by De Luca and Marano (2012). Both studies report an increase in the load-bearing capacity, stiffness, and ductility of the post-tensioned beams compared to reference beams without post-tensioning.

In addition, the application of post-tensioning to other wood-based materials has been investigated. Gessner et al. (2019) investigated post-tensioned dowel laminated timber elements and Gräfe et al. (2018) investigated post-tensioning of cross-laminated timber (CLT) elements. The use of alternative materials for post tensioning of timber beams, such as glass fibers and carbon fibers, has been investigated by D'Aveni and D'Agata (2017), giving also a summary of previous studies in this field.

2 Bonding behaviour

2.1 Material and Methods

Push-out (Figure 1 a/b) and pull-out tests (Figure 1 c/d) were performed to investigate the bonding behavior between the tendon, the inner grout (tendon to duct), the duct, the outer grout (duct to timber), and the surrounding timber. All tests were performed at ETH Zurich using a universal testing machine of type Schenck Hydropulse with a force capacity of 480 kN.

The specimens (300 x 300 x 110 mm^3) were produced from Norway spruce (*Picea abies* H. KARST.) glulam of strength class GL24h. The average moisture content (MC) during the tests was MC = 10.4%. For the inner grout between tendon and duct, cementitious injection mortar of type VSL-HPI® was used in all cases. For the grout between duct and timber, either the same mortar (VSL-HPI®) or GSA-adhesive® (two component epoxy adhesive) was used. Two milling sizes of 80 x 80 mm^2 and 140 x 140 mm^2 were investigated (Figure 2). The milling was done either with a flat surface (Figure 2a, indicated with *G* in Table 1) or with a notched surface (Figure 2b, indicated with *N* in Table 1).

The initial global stiffness parameter $k_{glob,1}$, the reloading global stiffness parameter $k_{glob,2}$, and the ultimate failure load F_{ult} were determined for each specimen. The ultimate failure load per m' length ($F_{ult'}$) was derived. An overview of the test program can be found in Table 1.

In both the push-out and the pull-out tests, the specimens were installed centrically in the Schenk Hydropulse. For the push-out test (Figure 1 a/b), the load was applied directly from the calotte to the protruding tube filled with mortar to the top. In the pull-out tests, the support was installed at the upper surface with steel parts pulled down by threaded rods. The anchor head was clamped in the testing machine and the strands were pulled upwards.

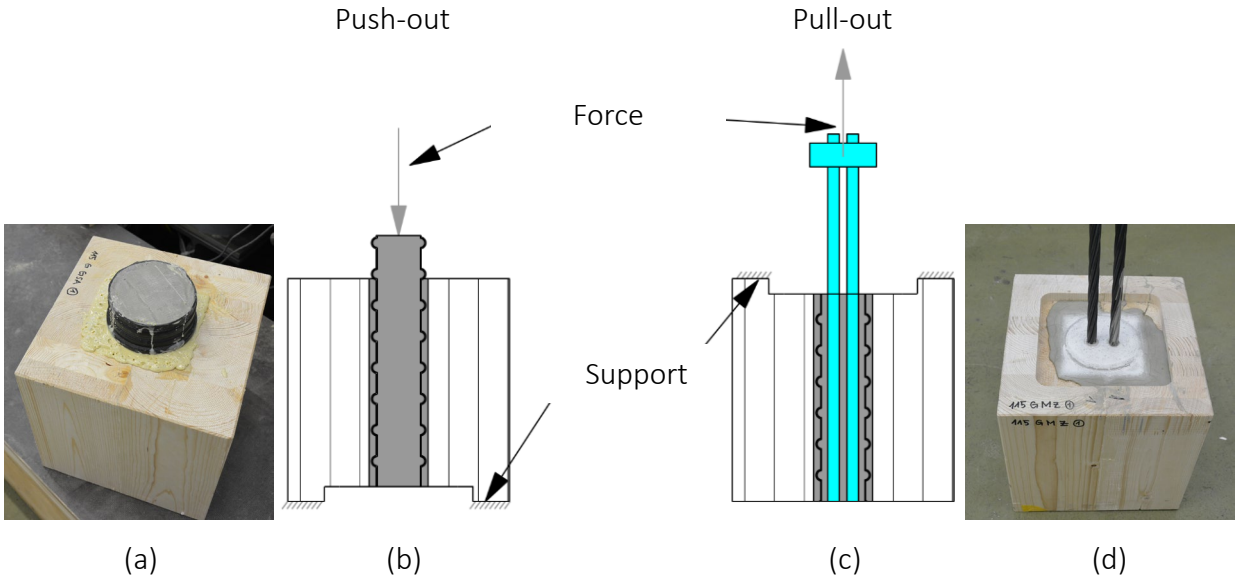

Figure 1: Push-out (a/b) and pull-out (c/d) test configuration.

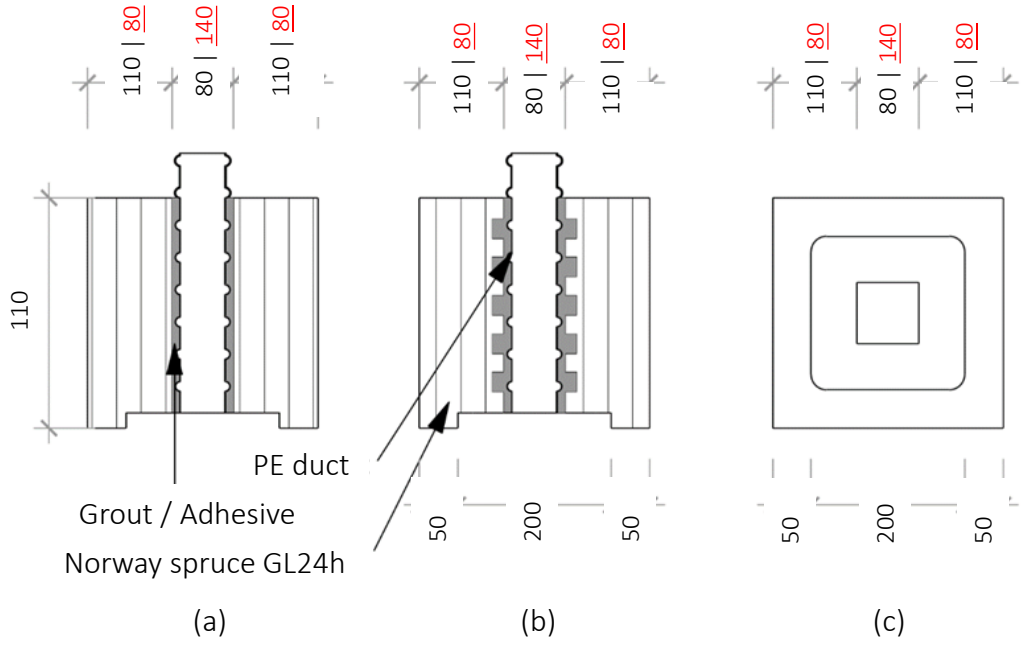

Figure 2: Geometry of the push-out and pull-out test specimens featuring the Norway spruce glulam block (300 x 300 x 110 mm³) and the grouting zone (80 x 80 or 140 x 140 mm²), a flat (a) or ribbed (b) milling surface, and the corrugated polymeric duct.

To determine the compressive strength of the mortar, additional specimens were produced and tested separately.

2.1.1 Push-out tests

The measuring equipment consisted of a load cell in the testing machine and LVDTs (linear variable differential transformer) to measure (i) the stroke way of the hydraulic jack, (ii) the deformation between the hydraulic jack, and the upper surface of the timber part, and (ii) the differential deformation between the lower surface of the timber part and the mortar inside the duct.

The force was applied displacement controlled with a rate of 0.008 mm/s. In a first cycle, 40% of the expected failure load were applied and again reduced to 10%. This cycle was used to determine the initial global stiffness parameter ($k_{glob,1}$). Subsequently, the load was increased until failure occurred or until the plateau was reached and the force dropped to 80% of the ultimate force (F_{ult}).

The global stiffness parameter (k_{glob}) shown in Table 1 was determined with the measured force of the load cell and the deformation of the hydraulic jack. Hence, it is not directly possible to determine the bonding stiffness. This was done with the numerical model shown in Section 2.3.

2.1.2 Pull-out tests

For the pull-out tests, the same measuring equipment was used as in the push-out tests (section 2.1.1). The lower LVDT was placed on one of the strands at the bottom to detect a pulling-in of the strands. The load cycles were also performed in the same way. Due to the lower stiffness of the specimens, the force application rate was increased to 0.01 mm/s.

2.2 Results

Table 1 summarizes the main test results of the push-out and pull-out tests, i.e., the initial global stiffness parameter $k_{glob,1}$, the reloading global stiffness parameter $k_{glob,2}$, and the ultimate failure load F_{ult}.

Table 1: Test programme and results of the push-out and pull-out tests including the number of specimes (n), the global stiffness (mean values) of the first ($k_{glob,1}$) and second load application ($k_{glob,2}$), the ultimate failure load (F_{ult}) and the failure load per m length (F_{ult}').

	Series [-]	Milling size [mm]	Milling type [-]	*n* [-]	Grout [-]	$k_{glob,1}$ [kN/mm]	$k_{glob,2}$ [kN/mm]	$F_{ult,mean}$ [kN]	$F_{ult,mean}$' [kN/m]
push-out	59 G-M	80 x 80	flat	3	mortar	122	163	146	520
	59 N-M	80 x 80	notched	3	mortar	114	154	164	587
	59 G-GSA	80 x 80	flat	3	GSA	99.6	153	160	570
	115 G-M	140 x 140	flat	3	mortar	204	-	178	634
	115 N-M	140 x 140	notched	3	mortar	190	-	285	1018
	115 G-GSA	140 x 140	flat	2	GSA	163	157	327	1166
pull-out	59 G-M-Z	80 x 80	flat	3	mortar	26.1	40.6	49.3	176
	59 N-M-Z	80 x 80	notched	3	mortar	27.1	21.6	95.2	340
	115 G-M-Z	140 x 140	flat	3	mortar	26.7	66.0	85.8	303
	115 N-M-Z	140 x 140	notched	3	mortar	21.9	59.4	126	450

2.2.1 Push-out test results

The specimens generally showed a ductile behavior (Figure 3). However, a closer look revealed that the ductility in specimens with notches and mortar filling 59 N-M (Figure 3c) and the specimens without notches and adhesive filling 59 G-GSA (Figure 3e) was due to the compression failure of the mortar at 58 MPa.

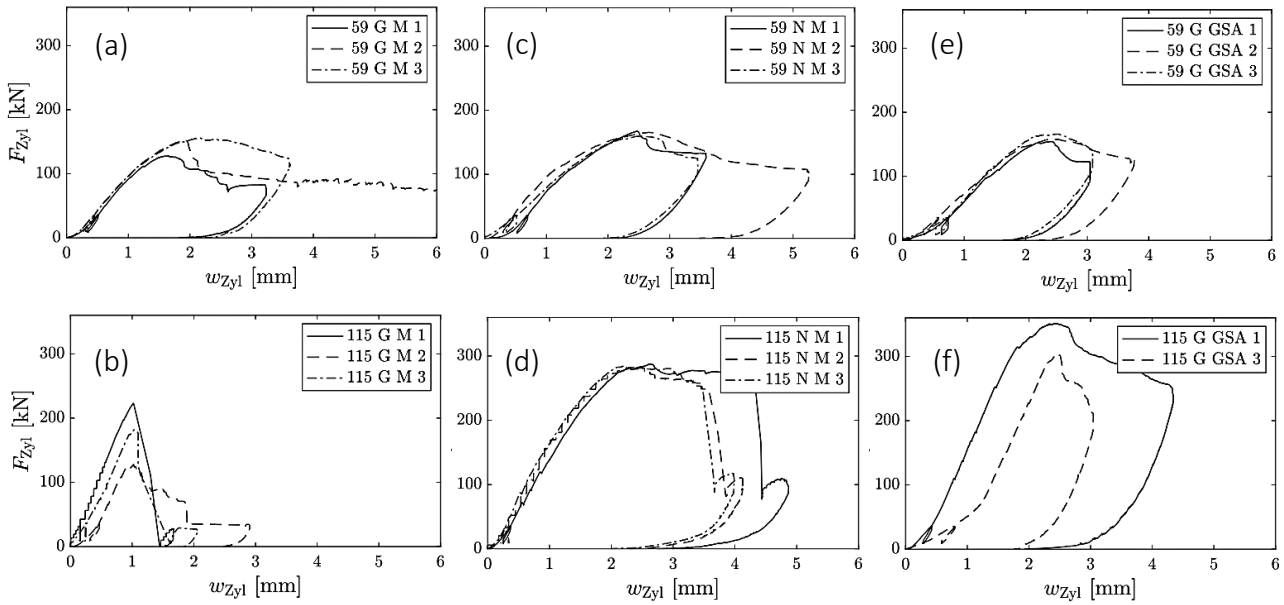

Figure 3: Force-displacement diagrams of the push-out tests. Specimens with mortar grout + without notches (G; a & b), with mortar grout + with notches (N; c & d), and with GSA adhesive grout + without notches (G; e & f) are shown.

This corresponds well with the determined compressive strength in the additional tests ($f_{c,mean}$ = 62 MPa). Specimens of the type 115 N-M (mortar filling & without notches, Figure 3d) failed due to vertical splitting of the timber part indicating a horizontal force in the timber part leading to stresses perpendicular to the grain. A bonding failure occurred as the mortar block drifted out of the timber part at a corresponding shear stress of 1.6 MPa in specimens of type 59 G-M (Figure 3a), at 1.1 MPa for 115 G-M (Figure 3b), and at 2.1 MPa for 115 G-GSA (Figure 3f).

2.2.2 Pull-out test results

The results summarized in Table 1 show that the pull-out specimens achieved a significantly lower failure load compared to the push-out tests of the same geometry (59 vs. 115). This circumstance can be explained by different failure mechanisms observed in the two test setups: All pull-out specimens showed a failure of the bonding between the mortar and the steel strands. Specimens of type 59 G-M-Z had one strand, types 59 N-M-Z and 115 G-M-Z two and type 115 N-M-Z had three strands.

The ultimate force observed in the tests showed an increase from one to two strands by a factor of 2.0 und from one to three strands by a factor of 2.6. There might be a group effect or different loading of the individual strands due to the slip in the anchor head. The specimens of type 115 N-M-Z showed a splitting of the timber part, similar to the failure observed in push-out tests with specimens featuring notches. It can be concluded that the stresses perpendicular to the grain introduced by the notches led to this failure. As these failure mechanisms are not in the scope of the project, the results will not be considered in the further analysis.

Due to the protruding length of the strands, the stiffness is significantly lower compared to the push-out tests.

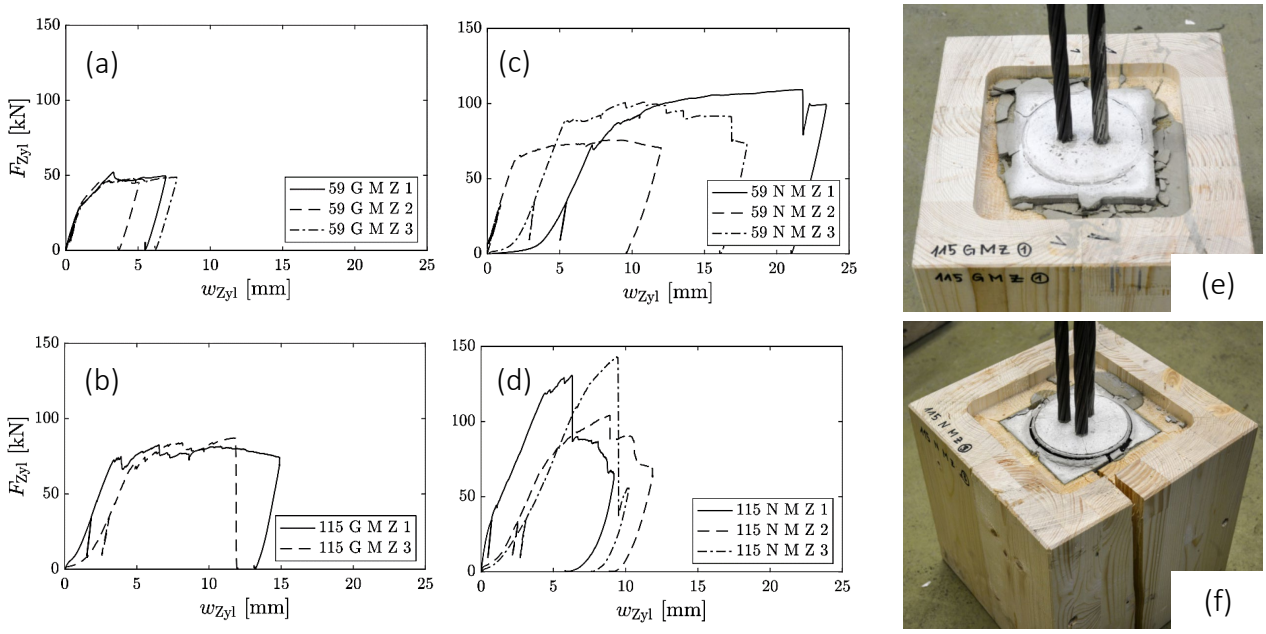

Figure 4: Force-displacement diagrams of the pull-out tests. Specimens with mortar grout + without notches (G; a & b) and with mortar grout + with notches (N; c & d) are shown. Failures of specimens without notches (115-G-M-Z; e) and with notches (115-N-M-Z; f) are shown on the right.

2.3 Discussion

Whereas the failure in the push-out tests occurred in the contact zone timber to mortar, in the pull-out tests a pulling out of the strands was observed. For specimens featuring notches, splitting of the timber was observed in several of the push-out as well as pull-out tests.

The bonding resistance between the surrounding mortar and the timber of the tested configuration was higher than the bonding resistance of the strands to the mortar. This can be explained by the larger contact area and differences in the interface shear strength. For a larger number of strands (type 59 can have up to 7 strands and type 115 up to 27 strands), higher bonding capacities are expected to occur.

With regard to the bending specimens and practical application, extrapolating the pull-out test results leads to a pull-out resistance of 280 kN for 7 strands and 1050 kN for 27 strands. For post-tensioned glulam beams with spans of 30 to 40 m (VSL type 6-55 with 45 strands), a bonding resistance of approximately 200 kN/m is required on design level according to *Bürgi* (2022). For the bending test described in section 3, a resistance of 80 to 100 kN/m is required. Hence, even the smaller duct diameter (type 59) with the simplest solution (G; without notches) achieved more than double the required bonding resistance per meter on a mean level (520 kN/m).

In order (i) to avoid introducing additional stresses perpendicular to the grain as observed for the notched configuration and (ii) to achieve simplifications in production it was decided (a) to proceed without notches in the milling and (b) to use cementitious mortar as the filling material. Although the GSA-adhesive showed an even higher resistance - exceeding the required performance unnecessarily - the application on a larger scale is considered much more difficult and costlier.

With a simple 2D numerical model, the shear stiffness between mortar and timber was simulated. For the specimens of type 59 G-M, a stiffness of 160 kN/mm was determined. This value will be used as an input parameter in the analytical and numerical modelling of the bending tests in Chapter 4.

3 Bending behaviour

3.1 Material and methods

The bending behavior was analyzed with tests on 11 specimens. Three main parameters were modified: (i) The timber species and strength class: Norway spruce (GL24h) and European ash (*Fraxinus excelsior* L., GL40h); (ii) The span and size: 7.20 m (h = 400 mm, b = 120 mm) and 10.50 m (600/150 mm); (iii) The bonding: no bonding between tendon (monostrands) and timber (unbonded) and bonding with mortar filling between tendon and corrugated flat duct and between duct and timber.

Different strength classes and wood species were used to validate the calculation approach on different failure load levels and to observe the predicted compression failure parallel to the grain on different materials.

Two different spans and cross-section geometries were tested to explore the influence of a possible volume effect. The tests of specimens with and without bonding should allow for the analysis of differences regarding the failure behavior, the bending stiffness, and the bending capacity.

3.1.1 Production of bonded and unbonded tendons

Each beam was produced in two halves, in which the openings were milled before block gluing them together (Figure 5a). Monostrands were inserted in this opening for the unbonded specimens. For the specimens with bonded tendons, the polymeric flat duct was mounted on one half before the block gluing. Parallel to mounting the duct, tension rings and sealings of the outer chamber were installed.

In Figure 5a, the two chamber openings for the injection of the cementitious mortar are visible. Initially, the inner opening closer to the center of the beam is used to fill the void between timber and duct (Figure 5b). After applying the post-tensioning, the outer chamber opening is used to fill the duct of the bonded tendons (Figure 5c).

3.1.2 Test set-up

Symmetric four-point bending tests according to *EN 408* (2010) were performed. The span of the beams with a height of h = 400 mm was l = 7.20 m (l/h = 18; Figure 6a) and the inner distance between the load application points was 2.40 m. For the beams with a height of h = 600 mm, the span was l = 10.50 m (l/h = 17.5) and the inner distance between the load application points was 3.48 m (Figure 6b). The rather unconventional dimensions were due to construction works at the lab at ETH Zurich.

The two hydraulic jacks were equipped with load cells and LVDTs in order to measure the vertical deformations. Additionally, vertical deformations were measured at the bottom side of the specimens in the center and 2.5 x h away from the center on each side. On both supports, horizontal deformations and vertical deformations of the timber beam due to compression stresses perpendicular to the grain were measured.

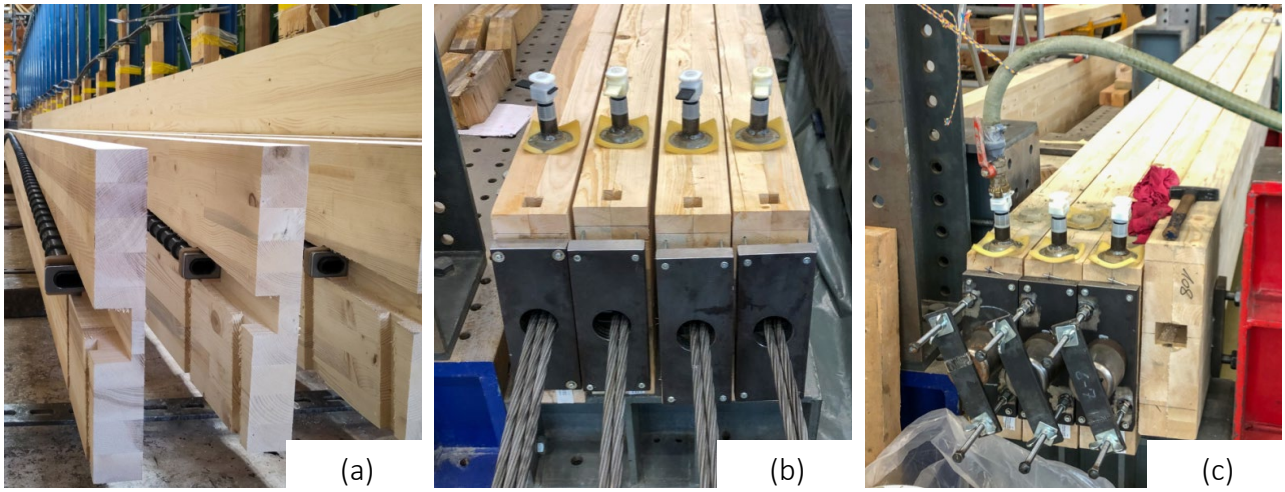

Figure 5: Half of Norway spruce timber beams with parabolic millings and flat duct (a), specimens after block-gluing and after the first injection (between the duct and timber) with mortar grout (b), and second injection (inside the duct) after appliying the post-tensoning (c).

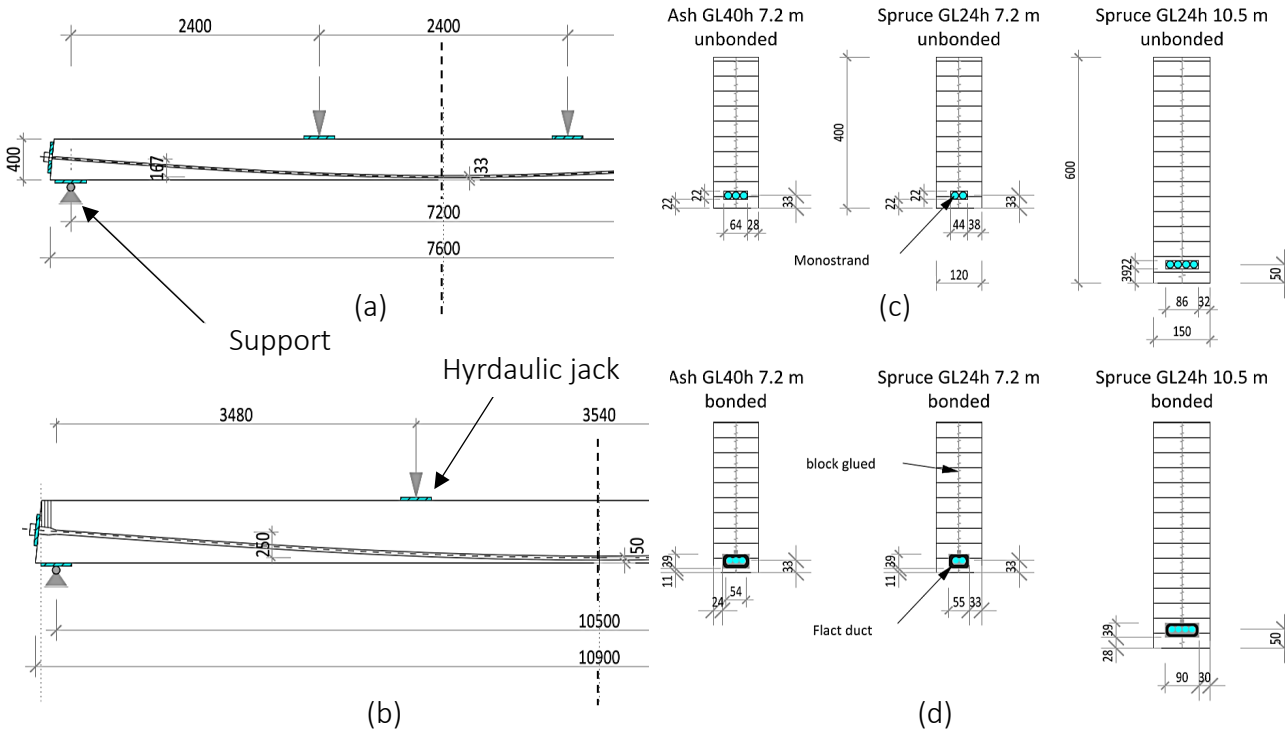

Figure 6: Dimensions and load application points of the four-point bending specimens with beam height of h = 400 mm (a) and 600 mm (b). The cross sections and types of monostrands of the unbonded (c) and flat ducts of bonded (d) Norway spruce and European ash specimens are shown.

For specimens without bonding, additional load cells were placed on both sides under the anchor head to measure the post-tension force and the loss of post-tension force from the active to the passive side.

One servo-hydraulic jack was controlled applying a constant displacement rate of 0.5 mm/s, for the second jack, the measured force of the first jack was applied.

3.1.3 Test protocol

Two load cycles up to 15% of the expected failure load were performed before and after activating the post-tensioning for direct comparison of its influence on the stiffness. LED markers placed on the glulam beams and the optical measurement system Optotrak Certus (NDI) were used to derive the modulus of elasticity.

The test protocol for the unbonded specimens consisted of the following steps: (i) Non-destructive four-point bending test of the specimen without post-tensioning to determine the bending stiffness of the timber beam. (ii) Post-tensioning of the beam to 180 kN post-tension force (F_{PT}) with fixed hydraulic jacks to measure the vertical (uplift) force on the hydraulic jack. (iii) Release of the hydraulic jacks and measurement of the vertical deformation (cambering), while increasing the PT force to the desired level. (iv) Destructive four-point bending test.

The approach for the bonded specimens was similar but the first non-destructive test was performed with the mortar of the outer chamber already grouted. The waiting / curing time between grouting of the outer chamber and non-destructive test and between grouting of the inner chamber and destructive test was 7 days each.

3.2 Results

3.2.1 Post-tensioning force during the application and during the tests

Figure 7a shows the force in the post-tensioning (PT) tendons (measured with the load cells at the beam's end). It can be seen that little to no deformation occurred in the first phase of applying the post-tensioning due to the blocking of the hydraulic jacks. Subsequently, the hydraulic jacks are lifted and negative displacement (upward bending) occurs due to the post-tensioning. In the next phase, the subsequent increase to the desired PT force is visible and, finally, the slight decrease of force due to the wedge seating in the anchor head is partly visible. This wedge seating is happening when PT force is transferred from the stressing equipment to the anchorage.

Figure 7b shows the increase of PT force for the unbonded specimens during the destructive four-point bending tests. First, a linear phase is visible where the PT force increases due to the elongation of the tendons as a result of the vertical deformation of the beam.

In the subsequent phase close to the ultimate failure load, a non-linear relation between the cylinder force and the PT force occurs for all specimens. In this phase, cracks occur and therefore the PT force increases whilst the cylinder force shows a rather constant level with small increases and decreases.

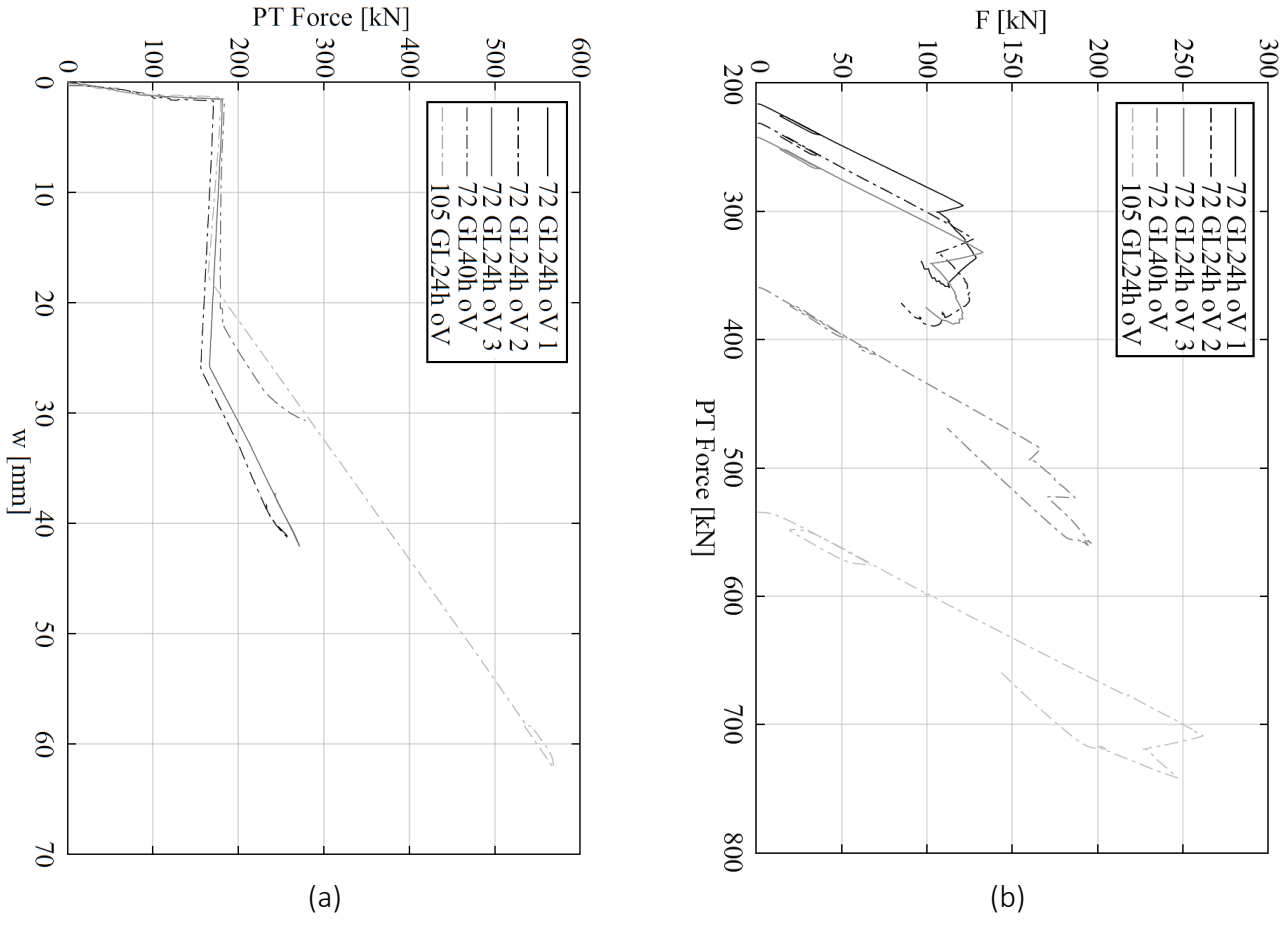

Figure 7: Development of the force in the post-tensioning cable F_{PT} for in the force application phase and for increasing deflections w (a) and as depeding on the cylinder force F (b).

3.2.2 Force-displacement behavior

The force-displacement behavior of the four-point bending tests is shown in Figure 8a (specimens without bonding) and Figure 8b (specimens with bonding). All specimens initially showed a linear elastic phase, followed by a highly non-linear phase.

The failures observed were either compression failures on the upper side of the beam or tensile failures at the bottom. Most specimens showed a softening after initial failures occurred.

Since the tests were performed deformation controlled, the ductility indicated by the curves shown in Figure 8 needs to be put in perspective. Not all specimens showed an increase of the bending resistance after the first cracks occurred (drops in the curves). However, an entirely brittle failure, i.e., a complete loss in bending resistance after the first failure, could not be observed. Additionally, the unloading paths show that all specimens (except 105 GL24 mV2, which was weakened during grouting) do have a significant residual load bearing capacity and stiffness.

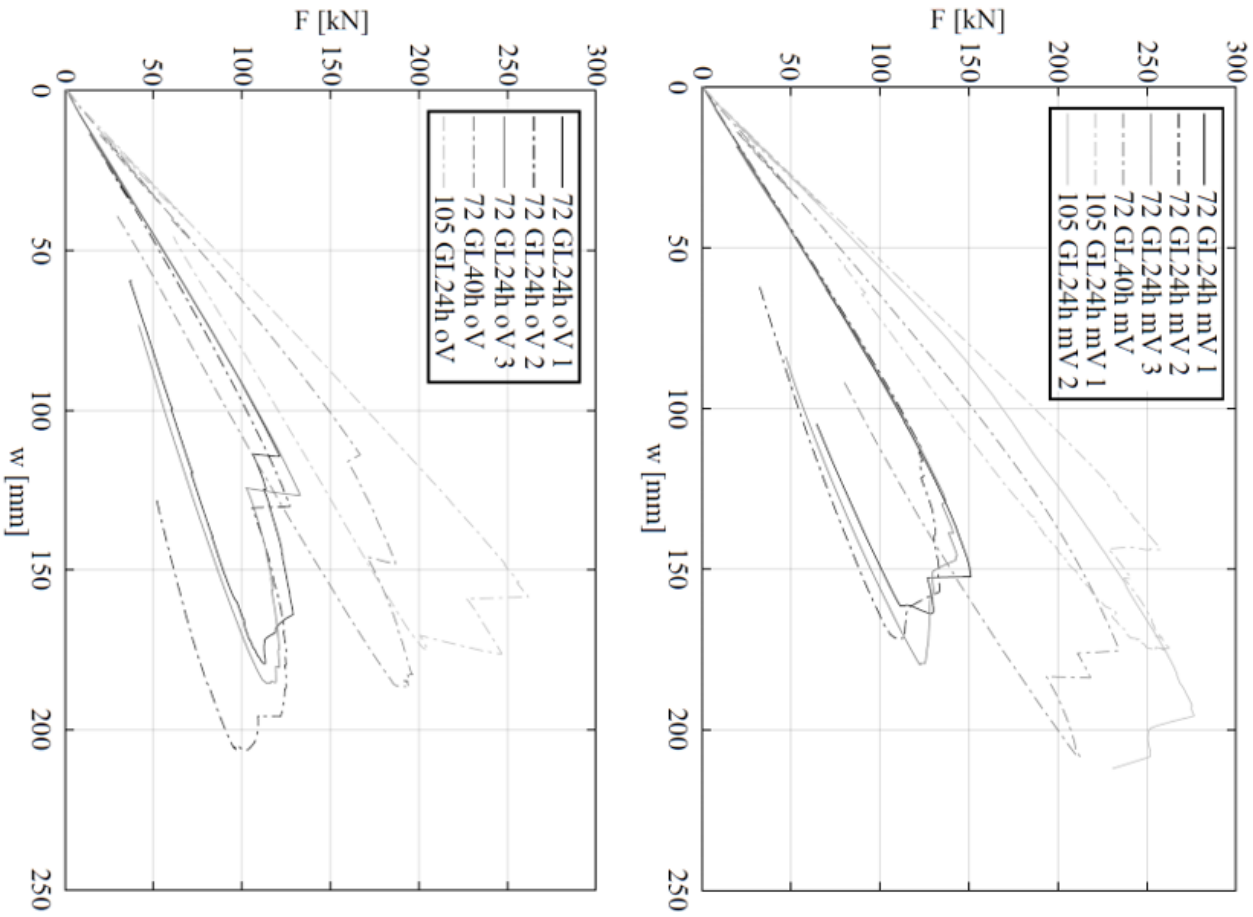

Figure 8: Force-displacement graphs of the Norway spruce (GL24h) specimens with a height of h = 600 mm, a span of 10.50 m with (mV) and without bonding (oV) (a) and of the Norway spruce (GL24h) and European ash (GL40h) specimens with a heigth of h = 400 mm and span of 7.20 m (b).

Table 2 summarizes the main results of the four-point bending tests. The rows EI_{GL}, EI_{PT} and Δ_{EI} show the bending stiffness of each of the specimens without and with post-tensioning. The unbonded specimens of strength class GL24h (Norway spruce) show an increase of 11.6% in bending stiffness (without PT vs. with activation of PT), while the bonded specimens of GL24h show an increase of 21.4%. The behavior of the European ash specimens (GL40h) is similar (+14.6% and +23.1%).

The rows $F_{PT,init}$ and $F_{PT,fail}$ list the values also visible in Figure 7b, where $F_{PT,fail}$ is the PT force just before the first failure or drop in the load-displacement curve occurs. Considering the load bearing capacity, the ultimate failure load (F_{ult}) of specimens of series 72-24h-oV and 72-24h-mV show little scatter within their group.

Table 2: Main results of the four-point bending tests on Norway spruce (GL24h) and European ash (GL40) glulam without (oV) and with bonding (mV). The bending stiffness before (EI_{GL}) and after post tensioning (EI_{PT}) is shown as well as the force in the tendon before applying the vertical forces ($F_{PT,init}$) and at the failure load F_{ult} ($F_{PT,fail}$).

Series [-]	h [mm]	No. [-]	EI_{GL} [MN/m^2]	EI_{PT} [MN/m^2]	Δ_{EI} [%]<	$F_{PT,init}$ [kN]	$F_{PT,fail}$ [kN]	F_{ult} [kN]
72-24h-oV	400	1	6.1	6.7	10.4	245	337	129
		2	5.7	6.3	11.0	245	322	127
		3	6.1	6.8	10.8	245	331	133
72-24h-mV	400	1	5.7	6.8	20.7	245	-	151
		2	5.7	7.0	23.4	245	-	134
		3	5.6	6.9	22.7	245	-	143
72-40h-oV	400	1	8.2	9.4	13.8	356	558	196
72-40h-mV	400	1	7.8	9.6	23.8	356	-	234
105-24h-oV	600	1	27.8	31.7	14.0	543	709	262
105-24h-mV	600	1	28.9	35.0	21.1	461	-	264
		2	29.4	35.0	18.9	521	-	276

3.3 Failure behavior, difficulties and discussion

The parabolic shape of the post-tensioning tendons leads to stresses parallel and perpendicular to the grain. On the one hand, pure compression acts on the beam and on the other hand, due to the uplift, reversed bending stresses occur compared to the subsequent stress in the four-point bending test. After applying the post-tensioning force, specimens of type 72-24h-oV had a tensile bending stress at the top of approximately $\sigma_{m,0,top}$ = 7.7 MPa and a compressive bending stress at the bottom of $\sigma_{m,0,bottom}$ = -17.9 MPa. During the destructive four-point bending test, these stresses are compensated first. Since the stresses from post-tensioning are lower on beams' top (later compression side), the failure is provoked in this zone.

Distinguishing between failures on the compression and tension side was generally difficult. With the data from the NDI, initiating compressive failures could be detected before tensile failures occurred. These zones of compression failures further emerged after tensile failure occurred, leading to a softening (see Figure 9a & b).

Due to the constant bending moment between the hydraulic jacks resulting from external forces in the four-point bending test and the parabolic bending moment due to the post-tensioning, the expected failure zone is not in the center of the beam but rather between mid-span and the hydraulic jacks.

Tensile failures occurred in the perimeter of the internal openings and included two to three of the lowest lamellae. The beams were designed with a minimal covering of timber around the carved openings for the duct. This geometry led to stress concentrations, provoking tensile failures in several cases.

Figure 9f shows the splitting of the two block-glued halves of a specimen of type 72-40h-mV (ash glulam with a span of 7.20 m with bonding). A small gap that was already visible a few days after grouting opened during the test. Although this phenomenon did not mark the ultimate load bearing capacity of the beam it contributed to a decrease of the activation of the bonded post-tensioning.

For the two specimens with a span of 10.50 m (Norway spruce, h = 600 mm), difficulties during post-tensioning and grouting were experienced. Both specimens showed cracks perpendicular to the grain during post-tensioning. Instead of the targeted PT force of F_{PT} = 564 kN, the PT force was limited to but to 521 and 461 kN respectively due to these cracks.

During the grouting of the outer and inner void, in several specimens cracking sounds were audible. Additionally, a partial splitting occurred close to the support on the other side of the grout inlet for the specimen 105-24h-mV-2 (Norway spruce, h = 600 mm) during grouting of the inner duct. This failure was due to the grouting pressure, which was set at 5 bar (usual pressure for PT tendons in concrete structures). The specimen was repaired with inclined screws and could be tested anyways. The second specimen of the same type (105-24h-mV-1) was grouted later, and the maximum pressure was limited to 2 bar. With this measure, no cracks occurred.

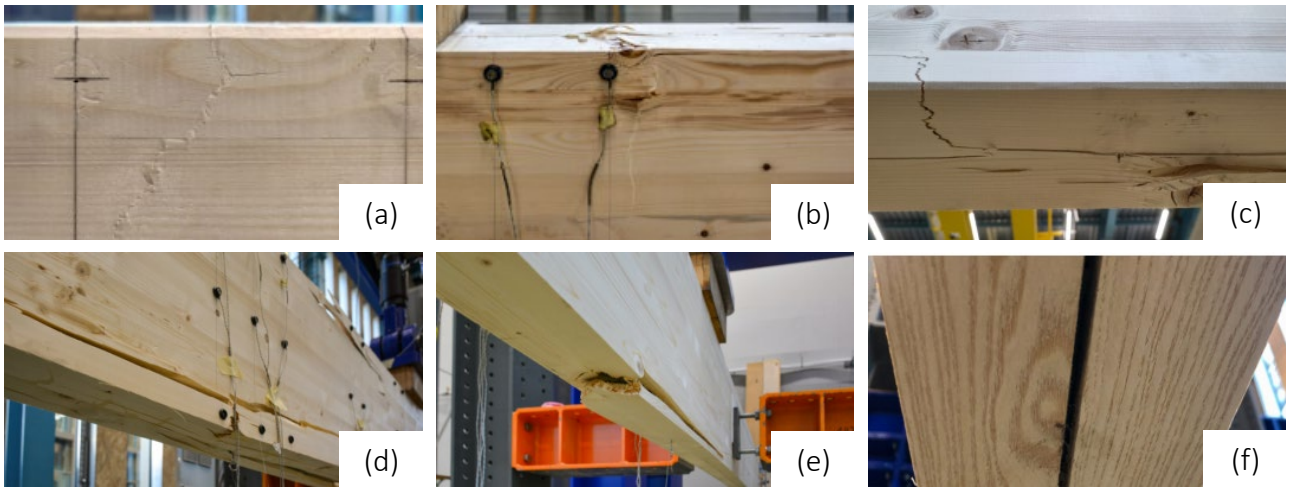

Figure 9: Failure patterns observed in the four-point bending tests: Failure in the compression zone of a Norway spruce glulam beam without (a) and with bonding (b), failure in the tension zone (c-e) and splitting of an ash glulam beam at the block gluing (f).

4 Modelling und Design

4.1 Numerical model

The specimens of the bending test were modelled as shell elements. The post-tensioning was coupled to the glulam beam with a hinged rigid member to analyze unbonded beams. For the bonded system, the tendons were coupled directly with the beam. Therefore, no bonding stiffness was considered between the tendons and the glulam beam. To calculate the acting stresses for the bonded specimens at ultimate load, the results of the two models were superimposed.

4.2 Analytical model

The post-tensioning was considered as an external force in the analytical model. On both ends of the beam, a horizontal force acts and a vertical (upward) force acts along the tendons onto the beam. For the unbonded systems, the increase of PT force was calculated with the elongation of the tendons due to the vertical displacement of the beam with Equation 1:

$$\Delta s = l + \frac{8}{2} \times \frac{\Delta f^2}{l} \tag{1}$$

Where Δs is the difference in length of the tendons (in mm), *l* is the length of the beam and Δf is the difference in height of the parabola or the vertical displacement. Several iterations are necessary to find the final equilibrium. In addition, the bonded system was modelled as a composite beam, considering the bonding stiffness between the timber beam and the steel tendons.

4.3 Comparison to experimental results

With the measured load at the occurrence of the first failure the acting stresses were calculated. In the following, only the stresses from the numerical model will be considered but the results of the analytical model matched the ones from the numerical model. On the compression side, the verification based on *SIA 265* (2021) was used:

$$\left[\frac{\sigma_{c,0,d}}{f_{c,0,d}}\right]^2 + \frac{\sigma_{m,y,d}}{f_{m,y,d}} \leq 1 \tag{2}$$

On the tension side, the compressive stress and the tensile bending stress were superimposed and compared to the bending strength. The mean values of Norway spruce GL24h were used according to *Blank* (2018) ($f_{m,mean}$ = $f_{c,0,mean}$ = 30 MPa). Material tests on specimens cut from the tested four-point bending specimens are planned in order to reduce the uncertainties related to the material properties.

A mean utilization factor over all specimens of 1.2 for the compression side at the first failure was determined. This factor is about 1.6-times higher than the utilization factor on the tension side supporting the observations of failures as a result of the compressive stresses parallel to grain.

Based on the same bending strength, a comparison of the measured ultimate load of the post-tensioned beams with the theoretical ultimate load of beams without post-tensioning was done. For GL24h, post-tensioning of the glulam beams without bonding leads to an increase in the load bearing capacity by 64%. With bonding, an increase by 77% is determined.

4.4 Design recommendations

The load bearing capacity of the post-tensioned beams could be predicted conservatively with the two verifications given in section 4.3 . Equation 2 is applicable to post-tensioned timber beams, achieving a higher load bearing capacity compared to a simple superposition of external and internal stresses on the tension side. The vertical displacements due to the post-tensioning and due to the external forces can be described well with the two approaches.

The load introduction of the PT force was done with a 40 mm thick steel plate. The specimens with cross-sections of h x b = 400 x 120 mm showed no cracks perpendicular to the grain. To prevent the beams from cracking, as occurred in specimens 105-24h-mV-1 and 105-24h-mV-2, a load dispersion angle of 5° can be assumed and the stresses perpendicular to grain must be calculated on the cross-section weakened by the opening. In addition to this stress, the tensile stress perpendicular to the grain due to the uplift force has to be considered.

Designing the bonded beams with a rigid connection between the tendons and the glulam beam leads to a conservative approximation of the bonding shear force but, on the other hand, to an underestimation of bending stresses. Therefore, both scenarios should be analyzed independently.

5 Conclusion

5.1 General

The experiments presented in this paper confirm the potential of post-tensioned timber beams with parabolic shape of the tendons. The post-tensioning and grouting processes, along with suitable elements, were developed in cooperation with the companies VSL AG and Neue Holzbau AG. The load bearing capacity can be increased significantly with post-tensioning (up to +80% observed in this study). Regarding the bending stiffness, a considerable increase could be observed (+20%). Although the increase in the bending capacity and stiffness could also be achieved in a more cost-efficient manner by increasing the cross-section height or width, a controllable pre-camber and no deformation in the serviceability limit state as well as the possibility to achieve ductile failure mechanisms and a high residual load bearing capacity due to the catenary action can be arguments to further pursue the approach post-tensioned timber beams. Especially, if the beams have to be block-glued anyhow due to their dimensions.

5.2 Stiffness and load-bearing capacity

The measured increase in bending stiffness without bonding is 10 - 14% while the increase in bending stiffness with bonding is 20 – 23%. The theoretical increase in load-bearing capacity without bonding is 47 - 69%, while the theoretical increase in load-bearing capacity with bonding is 67 – 89%.

5.3 Verifications

5.3.1 General

The verification of the bending stress on the compressive side is too conservative. The interaction verification should be performed at this point. On the tension side, the verification of the bending stress should be carried out with the effective bending edge stress.

5.3.2 Limiting post-tension force

The sum of the tensile stresses perpendicular to the grain due to the uplift force on the residual cross-section next to the opening and the tensile stresses perpendicular to the grain due to the bursting forces should be limited to 0.5 N/mm^2.

Appendix

Publications

Marcel Muster, Thomas Ehrhart, Muriel Althaus, Hansueli Küng, Peter Rogenmoser, Kevin Rahner, Adrian Gnägi, Andrea Frangi, *Post-tensioned glulam beams - Experimental investigations of bonded and unbonded systems*, International Network on Timber Engineering Research (INTER) 2023, Biel, 21.08 – 24.08.2023.

Marcel Muster, *Sporthalle in Zürich mit vorgespannten BSH-Trägern*, 27. Internationales Holzbau-Forum IHF 2023, Innsbruck, 29.11 – 1.12.2023.

Load-displacement

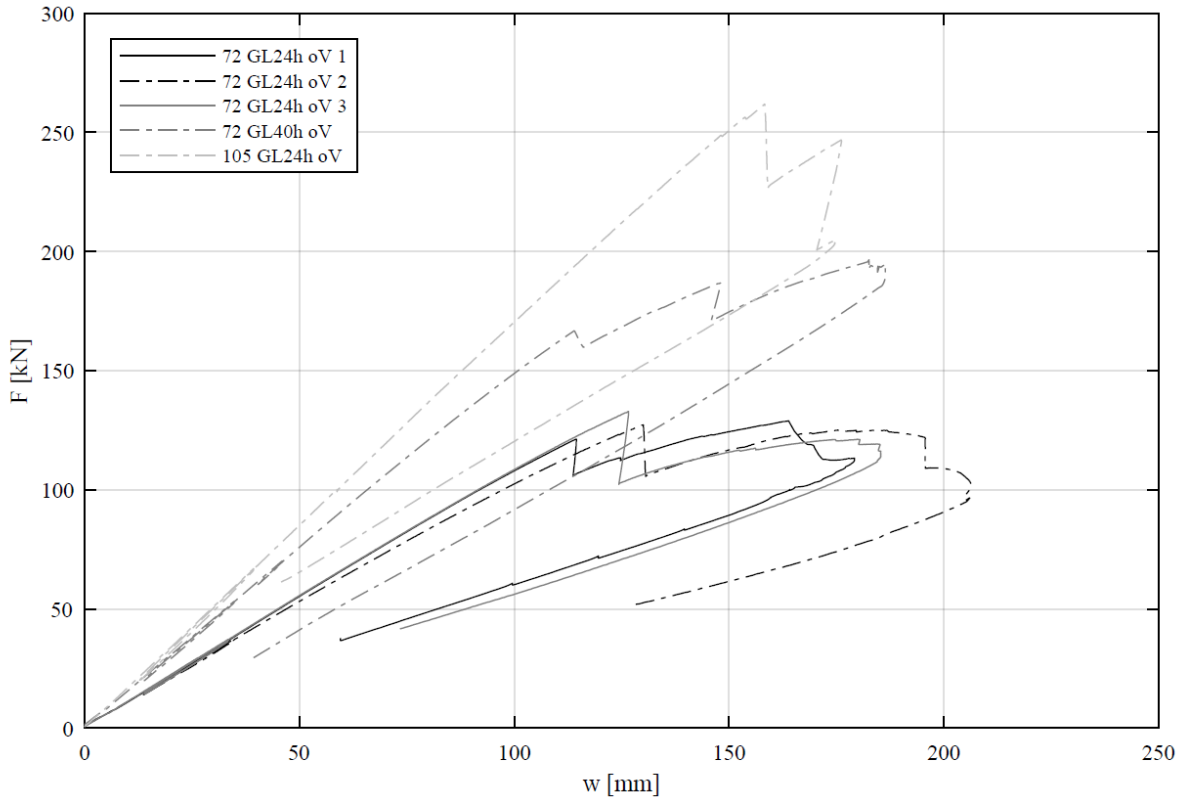

Abbildung 1 Bildlegende. Kraft (F = Gesamtkraft) zu Weg (w) für alle Prüfkörper ohne Verbund.

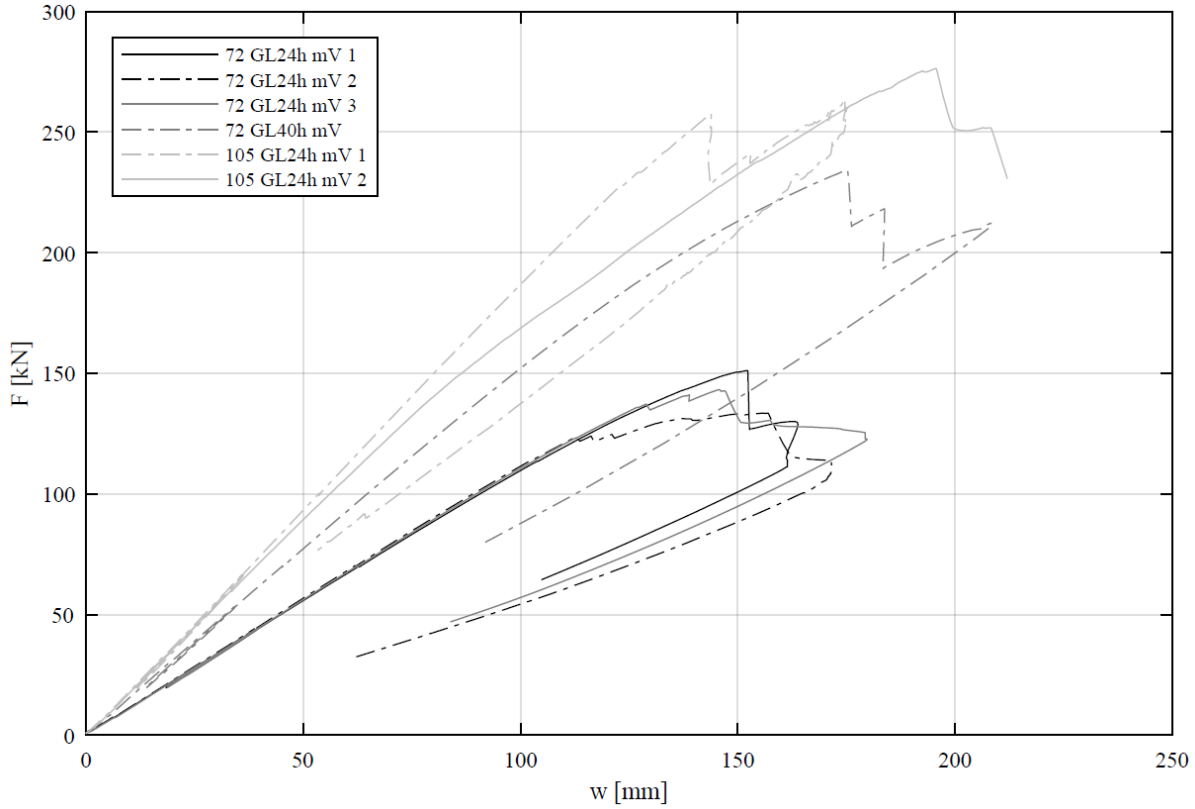

Abbildung 2 Bildlegende. Kraft (F = Gesamtkraft) zu Weg (w) für alle Prüfkörper mit Verbund.

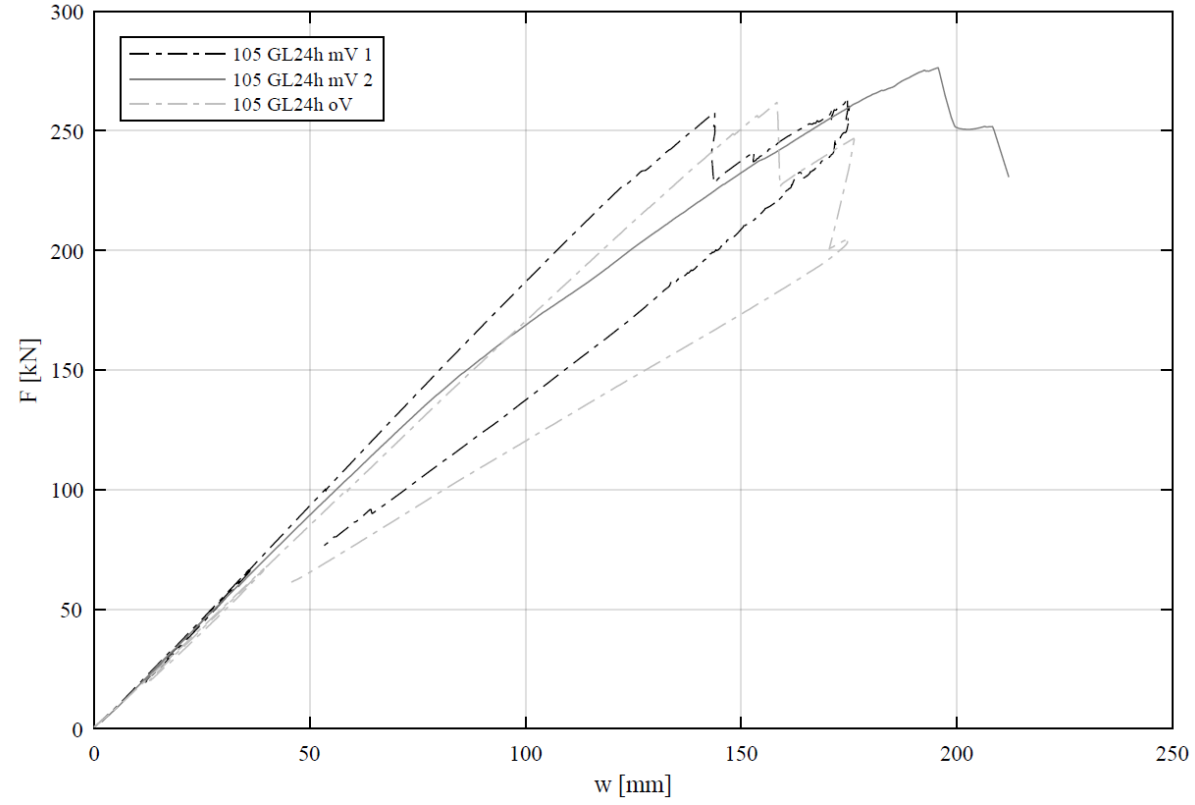

Abbildung 3 Bildlegende. Kraft (F = Gesamtkraft) zu Weg (w) für alle Prüfkörper mit 10.5 Meter Spannweite.

Post-tension froce

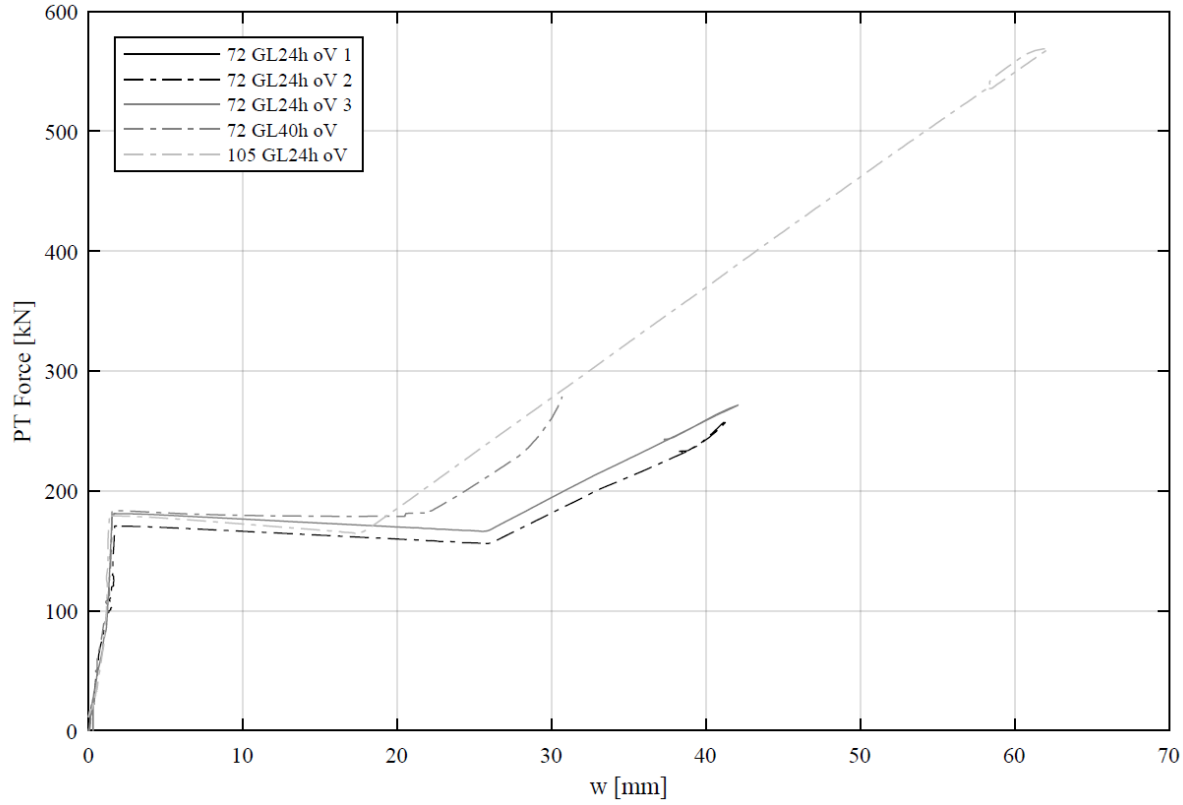

Abbildung 4 Bildlegende. Vorspannkraft (PT Force) gegen Weg nach oben in Trägermitte aller Träger ohne Verbund während dem Vorspannen.

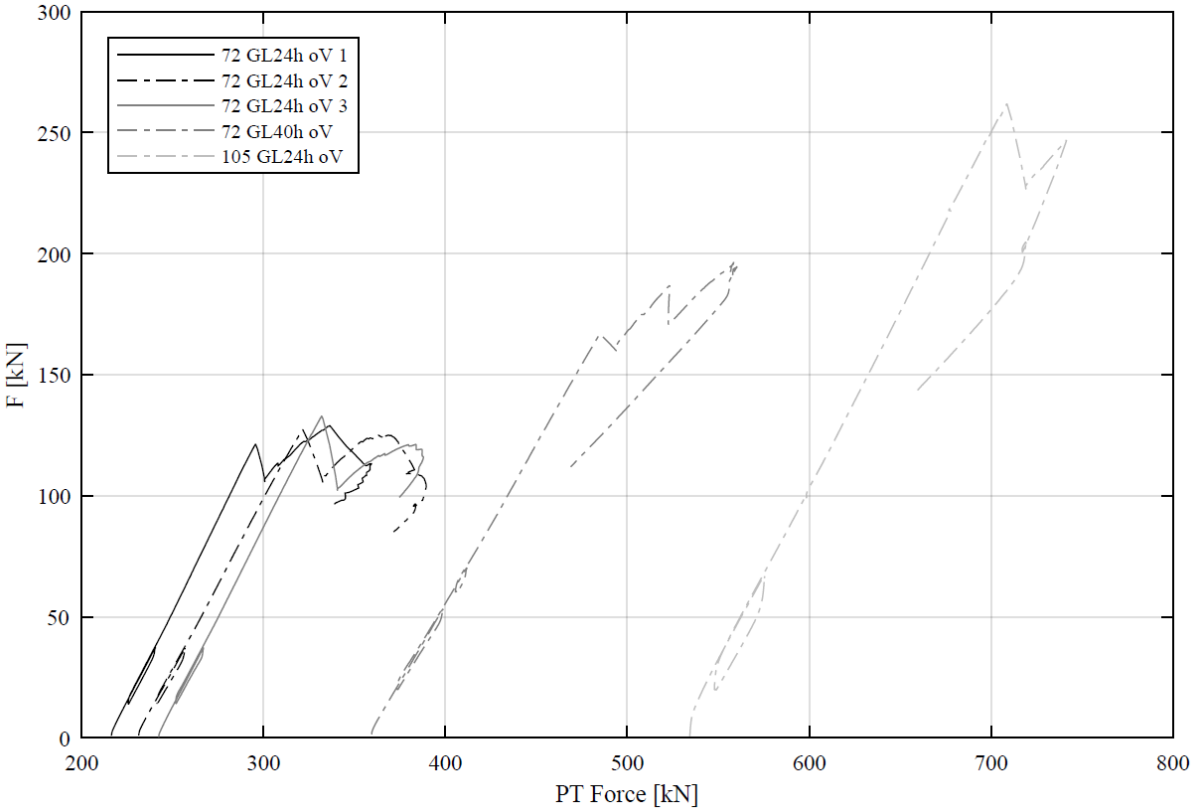

Abbildung 5 Bildlegende. Gesamtkraft (F) gegen Vorspannkraft (PT Force) aller Träger ohne Verbund während dem Vorspannen.

Steifigkeiten

Prüfkörper	EI BSH [Nmm²]	EI VG [Nmm²]	Unterschied [%]
72 GL24h oV1	6.1E+12	6.7E+12	10.4
72 GL24h oV2	5.7E+12	6.3E+12	11.0
72 GL24h oV3	6.1E+12	6.8E+12	10.8
72 GL24h mV1	5.7E+12	6.8E+12	20.7
72 GL24h mV2	5.7E+12	7.0E+12	23.4
72 GL24h mV3	5.6E+12	6.9E+12	22.7
72 GL40h oV	8.2E+12	9.4E+12	13.8
72 GL40h mV	7.8E+12	9.6E+12	23.8
105 GL24 oV	2.78E+13	3.17E+13	14.0
105 GL24 mV1	2.89E+13	3.50E+13	21.1
105 GL24 mV2	2.94E+13	3.50E+13	18.9

Kräfte

Prüfkörper	Vorspannkraft	Vorspannkraft bei Bruch	Bruchkraft
72 GL24h oV1	245.0	337.1	128.9
72 GL24h oV2	245.0	321.6	127.1
72 GL24h oV3	245.0	331.2	132.9
72 GL24h mV1	≈ 245.0	-	151.2
72 GL24h mV2	≈ 245.0	-	133.5
72 GL24h mV3	≈ 245.0	-	143.1
72 GL40h oV	355.9	558.2	195.7
72 GL40h mV	≈ 355.9	-	234.2
105 GL24 oV	543.0	708.8	261.9
105 GL24 mV1	≈ 461.0	-	263.5
105 GL24 mV2	≈ 521.0	-	276.2

Calculations

Vorgehen

Schritte

RFEM

1. Modell in welchem das Vorspannkabel nicht direkt mit der Fläche verbunden ist, sondern über Starrstäbe gekoppelt.

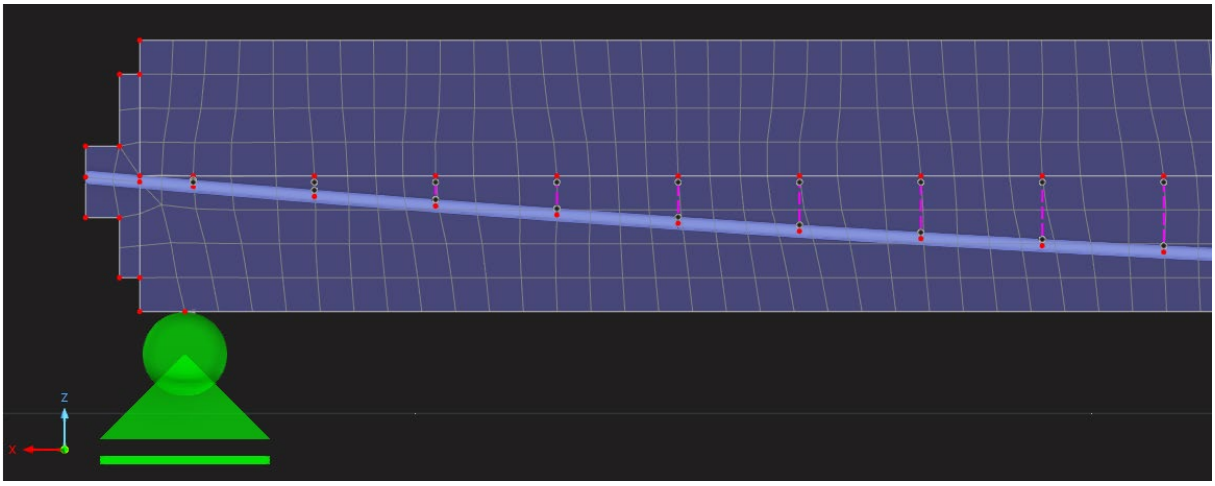

2. Vorspannkraft simulieren und Spannungen rauslesen: Randspannung oben und unten sowie Schwerpunktspannung (Druckspannung durch Vorspannung).
3. Falls ohne Verbund: In diesem Modell die vertikale Kraft aufbringen.
4. Falls mit Verbund: Neues Modell mit Vorspannkabel in Fläche integriert.

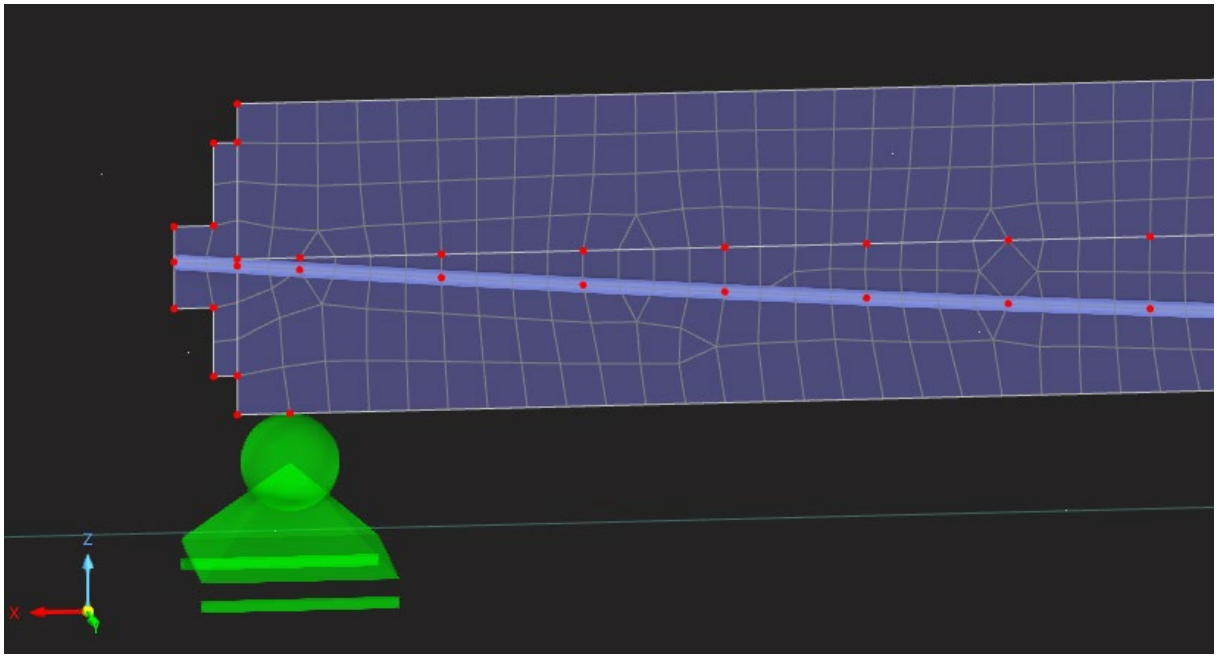

5. Belastund aufbringen und Spannungen rauslesen: Randspannung oben und unten sowie Schwerpunktspannung (Druckspannung durch Steigerung Vorspannung).

6. Nachweis Biegerandspannung oben: Sämtliche Spannungen überlagern
7. Nachweis Biegerandspannung unten: Sämtliche Spannungen überlagern
8. Nachweis Interaktion: Biegeanteile addieren (Randspannung minus Schwerpunktspannung), Schwerpunktspannungsanteile addieren.

$$\left[\frac{\sigma_{c,0,d}}{f_{c,0,d}}\right]^2 + \frac{\sigma_{m,y,d}}{f_{m,y,d}} + \frac{\sigma_{m,z,d}}{f_{m,z,d}} \leq 1$$

Handrechnung

1. Trägheitsmoment Träger mit Öffnung berechnen.
2. Trägheitsmoment Verbundträger mit Vorspannkabel berechnen.
3. Spannungszustand durch Vorspannung mit 1. Trägheitsmoment berechnen.
4. Spannungszustand Belastung mit 2. Trägheitsmoment berechnen.
5. Ohne Verbund: Zunahme Vorspannkraft berechnen über Verlängerung Kabel:

Rope length:
approx. first term of taylor apporx of this shape

$$s \cong l + \frac{8}{3} \cdot \frac{f^2}{l}$$ if f < /10

Daraus die neue Umlenkkraft berechnen: Iteration erforderlich, für die Durchbiegung des Trägers (Verkürzung des Trägers aufgrund der Druckkraft nicht berücksichtigen).

6. Nachweise gemäss 6., 7. und 8. oben

Material

Holz

Prüfkörper	fm,m	fc,0,m	fv,m
GL24h	30.0	30.0	3.4
GL40h	50.1	42.6	6.0

Verbundwirkung für analytische Berechnung: nc = 0.85

➔ Aus Push-out Versuchen, Bestätigt mit Biegesteifigkeiten in 4-Punktversuchen.

Steifigkeit Mörtel = 0 → Annahme gerissen

Resultate

Spannungen im Bruchzustand

	Analytisch			FEM		
Prüfkörper	σ_{top} [N/mm^2]	σ_{bot} [N/mm^2]	σ_{PT} [N/mm^2]	σ_{top} [N/mm^2]	σ_{bot} [N/mm^2]	σ_{PT} [N/mm^2]
72 GL24h oV1	-44.9	32.0	-7.0	-40.3	24.7	-6.8
72 GL24h oV2	-44.9	32.0	-7.0	-40.3	24.7	-6.8
72 GL24h oV3	-44.9	32.0	-7.0	-40.3	24.7	-6.8
72 GL24h mV1	-39.2	19.4	-5.3	-43.8	26.3	-5.1
72 GL24h mV2	-39.2	19.4	-5.3	-43.8	26.3	-5.1
72 GL24h mV3	-39.2	19.4	-5.3	-43.8	26.3	-5.1
72 GL40h oV	-59.5	37.2	-11.9	-51.1	26.8	-10.2
72 GL40h mV	-66.2	33.4	-7.9	-68.4	42.5	-7.4
105 GL24 oV	-48.4	29.7	-10.0	-40.9	21.7	-7.6
105 GL24 mV1	-38.1	18.5	-5.3	-38.1	23.3	-5.3
105 GL24 mV2	-39.3	17.9	-6.0	-39.4	23.0	-5.8

Ausnutzung im Bruchzustand

	Analytisch			FEM		
Prüfkörper	σ_{top}	σ_{bot}	Interaktion	σ_{top}	σ_{bot}	Interaktion
72 GL24h oV1	1.50	1.07	1.32	1.34	0.82	1.17
72 GL24h oV2	1.50	1.07	1.32	1.34	0.82	1.17
72 GL24h oV3	1.50	1.07	1.32	1.34	0.82	1.17
72 GL24h mV1	1.31	0.65	1.16	1.46	0.88	1.32
72 GL24h mV2	1.31	0.65	1.16	1.46	0.88	1.32
72 GL24h mV3	1.31	0.65	1.16	1.46	0.88	1.32
72 GL40h oV	1.19	0.74	1.03	1.02	0.53	0.87
72 GL40h mV	1.32	0.67	1.20	1.37	0.85	1.25
105 GL24 oV	1.61	0.99	1.39	1.36	0.72	1.17
105 GL24 mV1	1.30	0.60	1.12	1.30	0.80	1.12
105 GL24 mV2	1.30	0.60	1.15	1.30	0.80	1.20

Vorspannkräfte

Prüfkörper	Vorspannkraft	Vorspannkraft bei Bruch	Vorspannkraft bei Bruch RFEM
72 GL24h oV1	245.0	337.1	338.5
72 GL24h oV2	245.0	321.6	338.5
72 GL24h oV3	245.0	331.2	338.5
72 GL24h mV1	≈ 245.0	-	
72 GL24h mV2	≈ 245.0	-	
72 GL24h mV3	≈ 245.0	-	
72 GL40h oV	355.9	558.2	498.4
72 GL40h mV	≈ 355.9	-	
105 GL24 oV	543.0	708.8	724.8
105 GL24 mV1	≈ 461.0	-	
105 GL24 mV2	≈ 521.0	-	

Tragwiderstand

Prüfkörper	Bruchkraft mit VSP	BK ohne VSP	Unterschied
72 GL24h oV1	128.9	80.0	1.61
72 GL24h oV2	127.1	80.0	1.59
72 GL24h oV3	132.9	80.0	1.66
72 GL24h mV1	151.2	80.0	1.89
72 GL24h mV2	133.5	80.0	1.67
72 GL24h mV3	143.1	80.0	1.79
72 GL40h oV	195.7	133.3	1.47
72 GL40h mV	234.2	133.3	1.76
105 GL24 oV	261.9	155.2	1.69
105 GL24 mV1	263.5	155.2	1.70
105 GL24 mV2	276.2	155.2	1.78